High-Temperature Materials

SCIEPublish

Article

Ab Initio Molecular Dynamics Study of C_3S/CaO and C_2S/CaO Interfaces: Crystal Orientation Effects and Corrosion Mechanisms

Qingze Chen [1,†], Yidan Xing [1,†], Liang Huang [1,2,*], Haijun Zhang [1,2,*] and Shaowei Zhang [3]

[1] State Key Laboratory of Advanced Refractories, Wuhan University of Science and Technology, Wuhan 430081, China; chenqinze@wust.edu.cn (Q.C.); xing_ydan@163.com (Y.X.)

[2] International Joint Laboratory on New Technologies of Refractories and Metallurgy, National-Provincial Joint Engineering Research Center of High Temperature Materials and Lining Technology, Wuhan University of Science and Technology, Wuhan 430081, China

[3] College of Engineering, Mathematics and Physical Sciences, University of Exeter, Exeter EX4 4QY, UK; s.zhang@exeter.ac.uk (S.Z.)

* Corresponding author. E-mail: huangliang1986@wust.edu.cn (L.H.); zhanghaijun@wust.edu.cn (H.Z.)

† These authors contributed equally to this work.

Received: 12 July 2026; Revised: 31 July 2026; Accepted: 20 October 2026; Available online: 30 October 2026

ABSTRACT: MgO–CaO refractories exhibit significant potential in the cement industry owing to their excellent refractoriness, robust resistance to alkaline corrosion, superior coating adherence, and high thermodynamic stability. Nevertheless, the intricate interfacial interaction mechanisms between these refractories and cement clinker at high temperature remain poorly understood. In this study, *ab initio* molecular dynamics (AIMD) simulations were employed to investigate the interactions between various crystallographic surfaces of CaO and the two primary mineral phases of cement clinker (tricalcium silicate, C_3S, and dicalcium silicate, C_2S). The results demonstrate that the CaO(100) surface maintained interfacial structural stability through ordered coordination and minimal charge transfer. Conversely, the CaO(111) surface exhibits high interfacial reactivity and surface degradation, driven by its unstable surface structure and strong interfacial polarization effects. The interfacial reactivity of the CaO(110) surface is intermediate, suggesting that preferential exposure of the CaO(110) surface may improve the kiln coating performance of the refractory, nevertheless, this implication remains a theoretical prediction and requires further experimental validation. These findings offer fundamental atomic-scale insights for the optimization of MgO–CaO refractories in industrial cement production.

Keywords: CaO-based refractories; *Ab initio* molecular dynamics; Interface interaction; Cement clinker; Crystal facets

© 2026 The authors. This is an open access article under the Creative Commons Attribution 4.0 International License (https://creativecommons.org/licenses/by/4.0/).

1. Introduction

Owing to their superior high-temperature performance and good coating adherence, MgO–CaO refractories serve as critical linings for the burning and transition zones of cement rotary kilns [1–4]. Despite these merits, these refractories face serious challenges: the intense interfacial interactions and subsequent reactions occurring upon contact with cement clinker lead to refractory degradation, thereby curtailing service longevity and performance [5]. Prior investigations have demonstrated that during dynamic corrosion, the primary clinker phases react with the refractory to generate low-melting-point phases ($xCaO{\cdot}MgO{\cdot}ySiO_2$). The mutual diffusion of these species at the interface exacerbates clinker infiltration and accelerates structural disintegration. This interfacial instability not only disrupts continuous clinker production, but also presents substantial environmental challenges [6–10]. Therefore, extending the service life of refractory linings is important for reducing material consumption and kiln shutdowns [11–14].

Recent research concerning the interplay between cement clinker and MgO–CaO refractories has primarily focused on macroscopic corrosion behavior and the evolution of microstructures [15–17]. For example, Qiu et al. [18] demonstrated that C_2S reacts with free CaO to form a high melting point C_3S layer, which effectively hinders the inward diffusion of corrosive components such as Fe_2O_3 and Al_2O_3. Similarly, Rodríguez-Galicia et al. [19] observed that liquid clinker phases penetrate the refractory matrix along grain boundaries and pores, reacting to form a dense layer (approximately 600 μm) through a liquid-phase sintering mechanism. Although these studies provide valuable insights of the corrosion between clinker and refractories, they mainly rely on post-mortem characterization and cannot directly reveal the dynamic atomic-scale processes occurring at high temperature interfaces. In particular, how different CaO crystallographic facets regulate atomic diffusion, Si–O bond reconstruction, charge transfer, and interfacial stability during contact with C_3S and C_2S remain poorly understood.

Conventional post-mortem characterization can identify final reaction products, penetration depths, and corrosion morphologies, but it cannot resolve the temporal sequence of atomic diffusion, Si–O bond dissociation and reconstruction, and charge redistribution during the early stage of clinker refractory interaction. With advances in computational materials science, *ab initio* molecular dynamics (AIMD) has emerged as a powerful approach for probing atomic-scale processes that are difficult to access directly by conventional experimental techniques [20–27]. For instance, Liu et al. [28] utilized AIMD to investigate the high temperature interfacial interactions of molten Al with MgO surfaces of different crystallographic orientations. The results demonstrated that MgO(111) exhibited the strongest interfacial reactivity because of its high surface energy and highlighted the critical roles of crystallographic orientation and local chemical environment of refractory surfaces in regulating high temperature interfacial reactions. In a related AIMD study, Zhang et al. [29] used AIMD simulations to investigate the interfacial interactions between CMAS slag (47.5 wt% CaO, 8.0 wt% MgO, 39.5 wt% Al_2O_3, and 5.0 wt% SiO_2) and MgO surfaces with different crystallographic orientations. MgO(111) underwent pronounced atomic interdiffusion, charge redistribution, and severe surface disordering. The study further revealed that the interfacial behavior was controlled by the competition between stabilizing covalent Al–O networks and disorder promoting ionic redistribution involving Ca and Mg.

In general, the surface reactivity of CaO varies markedly with crystallographic orientation, which can substantially influence its interfacial interactions with cement clinker phases at high-temperatures. In addition, the major clinker silicate phases, tricalcium silicate (C_3S) and dicalcium silicate (C_2S), differ in their Ca/Si ratios and local structural environments, and may therefore exhibit distinct diffusion, bonding, and charge transfer behaviors upon contact with CaO surfaces. Consequently, it is necessary to clarify the coupled effects of CaO crystallographic orientation and clinker phase composition on atomic interdiffusion, interfacial Si–O bond reconstruction, charge redistribution, and surface stability. Such a mechanism is

essential for elucidating the atomic-scale mechanisms governing clinker adhesion and corrosion of MgO–CaO refractories under cement kiln conditions.

Accordingly, this work applies AIMD simulations to compare the high-temperature behavior of C_2S and C_3S in contact with three low-index CaO surfaces, specifically the (100), (110), and (111) surfaces. The structural evolution, atomic diffusion behavior, radial distribution functions, interaction energy, and electronic properties were systematically analyzed to clarify the interfacial reaction mechanism, thereby providing atomic-scale theoretical insights into the corrosion of MgO–CaO refractories.

2. Model Construction and Calculation Method

2.1. Interfacial Models

The CaO primitive unit cell was first optimized; as shown in Table S1, the optimized structural parameters are in excellent agreement with the reported reference values, confirming that the selected computational parameters are reasonable. All interface models were constructed by systematically expanding the primitive crystallographic unit cells into periodic supercells. Three intense diffraction peaks are observed in the XRD pattern of CaO, corresponding to the (200), (220), and (111) reflections (shown in Figure S1). Since the in-plane atomic configurations of the (200) and (220) planes in the cubic CaO lattice are identical to those of the (100) and (110) planes, respectively, the low-index planes (100), (110), and (111) were selected for interface construction. To represent the naturally predominant state, all surfaces were terminated by oxygen. Supercells were generated by cleaving along the corresponding orientations to expose the desired surfaces, resulting in CaO(100), CaO(110), and CaO(111) models containing 72 atoms (Ca_{36}, O_{36}) (shown in Figure S2). The atomic compositions of the C_3S and C_2S models are listed in Table S2. Each isolated mineral phase was initialized with a random atomic configuration and equilibrated by AIMD for 5 ps at 1873 K under periodic boundary conditions. Temperature and total energy exhibited stable fluctuations after approximately 3 ps (Figure S3). After 5 ps, the average Ca–O and Si–O bond lengths were approximately 2.25 and 1.65 Å, respectively, consistent with reported experimental values [3]. The equilibrated structures were then used to construct the C_3S/CaO and C_2S/CaO interface models. A series of interfacial configurations were constructed, each comprising C_2S or C_3S in contact with CaO surfaces by different low-index crystallographic surfaces, as shown in Figure 1. For clarity, the six interfacial systems were designated as C_3S/CaO(100), C_3S/CaO(110), C_3S/CaO(111), C_2S/CaO(100), C_2S/CaO(110), and C_2S/CaO(111), according to the crystallographic surfaces of CaO. To avoid artificial bonding and atomic overlap at the initial interface, a separation of 3 Å was maintained between the lower clinker (C_2S or C_3S) and upper CaO surfaces, supplemented by an additional 15 Å vacuum layer to eliminate interactions arising from periodic boundary conditions.

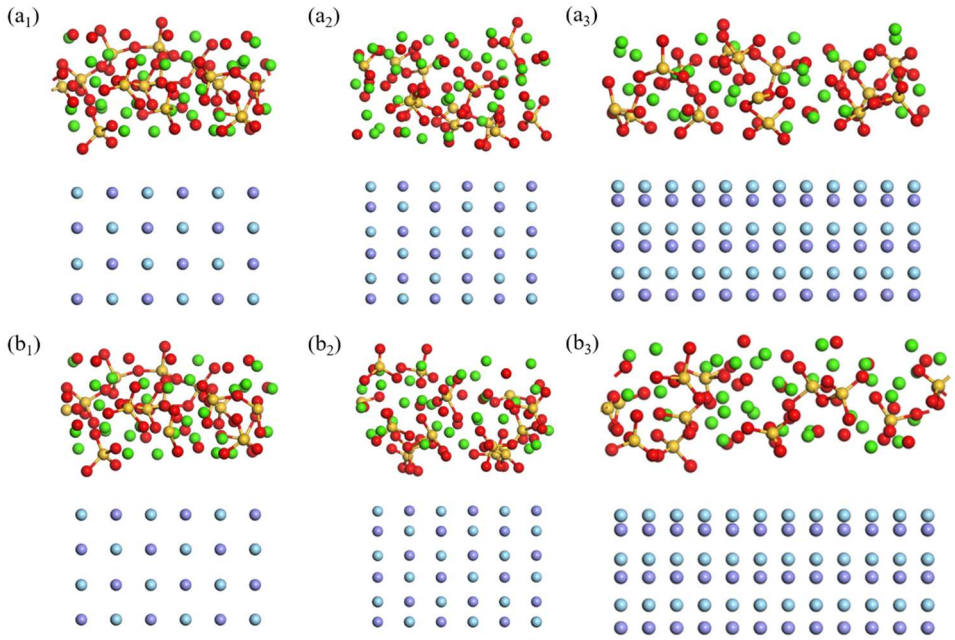


Figure 1. Interface models between C_3S/C_2S and CaO: (**a1**) C_3S/CaO(100), (**a2**) C_3S/CaO(110), (**a3**) C_3S/CaO(111), (**b1**) C_2S/CaO(100), (**b2**) C_2S/CaO(110), (**b3**) C_2S/CaO(111), (In the silicate phases, Ca, Si, and O atoms are shown in green, yellow, and red, respectively, whereas Ca and O atoms belonging to the CaO substrate are shown in purple and blue, respectively).

2.2. DFT Calculation and AIMD Simulation Methods

All structural optimizations were carried out within the plane-wave density functional theory (DFT) framework as implemented in the Vienna *Ab initio* Simulation Package (VASP) [30–32], using the projector augmented wave (PAW) method to solve the Kohn-Sham equations within DFT. The exchange-correlation potential used the Perdew-Burke-Ernzerhof (PBE) functional based on the generalized gradient approximation (GGA) [33,34]. The optimization parameters were set as follows: The convergence criteria for force and total energy were respectively set to 0.03 eV/Å and 1×10^{-4} eV. For DFT calculations, a plane-wave cutoff energy of 350 eV was adopted, and the Monkhorst–Pack k-point mesh was generated with a spacing of 0.04 $Å^{-1}$.

The AIMD simulations utilized the canonical ensemble (NVT), where the system maintains a fixed number of particles (N), volume (V), and temperature (T). The system temperature was regulated using the Nosé–Hoover thermostat [35]. The AIMD simulations were performed at 1873 K to examine clinker refractory interactions under a severe high-temperature condition representative of the kiln burning zone. During kiln operation, clinker contacts the refractory over a broader temperature range. The selected temperature therefore represents an upper temperature condition, rather than the initial contact temperature. A plane-wave cutoff energy convergence test was conducted prior to the production calculations. As shown in Figure S4, both the total energy and atomic forces exhibited only minor variations when the cutoff energy was increased beyond 350 eV, confirming that 350 eV provides an adequate balance between numerical accuracy and computational efficiency for the present AIMD simulations.

The simulation parameters were configured with a total simulation duration of 10 ps and time step of 2 fs (5000 steps). Owing to the relatively large size of the simulated interfacial systems, the AIMD calculations were carried out using $1 \times 1 \times 1$ Gamma-point sampling. Interfacial atomic density profiles and radial distribution functions (RDFs) were subsequently analyzed using the Visual Molecular Dynamics (VMD) package [26].

The atomic number-density distribution serves as a critical metric for quantifying atomic scale diffusion and can be calculated via Equation (1).

$$\rho(z) = \frac{N_z}{A_{xy} \triangle z} \tag{1}$$

where A_{xy} is the interface area; Δz represents the uniform bin thickness along the z-direction; and N_z denotes the average number of atoms contained within the slab between $z - \Delta z/2$ and $z + \Delta z/2$ during the sampling period.

The RDF was calculated according to Equation (2):

$$g(r) = \frac{dn(r)}{S(r)\rho dr}, S(r) = 4\pi r^2 \tag{2}$$

where, $dn(r)$ denotes the number of atoms distributed within a spherical shell with thickness dr at a radial distance r from the reference atom, $S(r)$ is the surface area of the spherical shell, and ρ is the atomic number-density of the system.

2.3. Calculation Methods for Electronic Structure and Energy Analysis

Although structural evolution, RDF analysis, and interaction energy characterize the extent and strength of interfacial reactions, they do not directly reveal the electronic origin of facet dependent reactivity. Therefore, charge density difference and Bader charge analyses were further performed to identify interfacial electron redistribution, clarify the electronic characteristics of newly formed Si–O bonds, and correlate atomic diffusion and local bonding reconstruction with interfacial polarization. Charge density difference (CDD) was calculated to elucidate the electron redistribution during interfacial interactions. Bader charge analysis was employed to quantify the electron transfer and estimate the valence states of individual atoms. Charge density difference and Bader charge were analyzed using VASPKIT (1.5.1) and VESTA (3.5.8) software [36–39].

The CDD was determined by using Equation (3):

$$\triangle \rho = \rho_C - \rho_A - \rho_B \tag{3}$$

where ρ_C is the total charge density of the integrated interface model, ρ_A is the charge density of the C_3S/C_2S, and ρ_B is the charge density of the CaO slab.

In addition, the surface energy reflects the surface activity of the material, which is calculated using the following formula:

$$E_{surface} = \frac{E_{total} - nE_b}{2S} \tag{4}$$

In the equation, E_{total} represents the total energy of the surface model, nE_b denotes the total energy of the corresponding bulk crystal that contains n primitive cells, and S is the surface area of the model (Surface energies of different crystal faces of CaO are shown in Figure S5).

Simultaneously, the interfacial interaction energy at the equilibrium state serves as a direct measure of the strength of interaction. It is determined by computing the difference between the energy of interfacial models and the energies of the C_2S/C_3S layer and the CaO substrate. The calculation formula is expressed as follows:

$$E_{Int} = \frac{1}{S}\left(E_{A/B}^{tot} - E_A^{tot} - E_B^{tot}\right) \tag{5}$$

In the equation, E_{Int} is the interfacial interaction energy per unit area of the interface, while $E_{A/B}^{tot}$ corresponds to the total energy of the interface system, E_A^{tot} and E_B^{tot} are the energies of the isolated A and B components, and S is the contact area of the interface.

3. Results

3.1. Interfacial Structural Evolution and Atomic Density

AIMD simulations were used to examine the behavior of the C_3S/CaO interfaces with different CaO crystallographic orientations at 1873 K (Figure 2). The simulation results demonstrate a strong dependence of interfacial chemical reactivity and atomic diffusion kinetics on the crystallographic orientation of CaO. For the (100) surface, the interface remains relatively stable: surface atoms of CaO(100) gradually deviate from their initial lattice positions and migrate toward the interfacial region, but they remain attached to the surface. Only a single Si atom from the C_3S phase forms a chemical bond with surface O atoms on the CaO substrate, resulting in the localized formation of a [SiO_4] tetrahedron at the interface. This restricted interfacial reactivity can be attributed to the low surface energy of the CaO(100) facet (0.61 $J \cdot m^{-2}$), which inherently dictates the lower chemical activity of the surface atoms. The CaO(110) surface exhibits intensified interfacial reactivity. Atoms from the CaO substrate are observed to migrate toward the interfacial region and detach from the surface lattice, accompanied by the formation of [SiO_4] tetrahedra at the interface (Figure 2b). This intensified reactivity is driven by the higher surface energy of the CaO(110) facet (1.46 $J \cdot m^{-2}$) compared to the (100) facet. Owing to its highest surface energy (3.88 $J \cdot m^{-2}$), the CaO(111) surface exhibits the most pronounced interfacial degradation. Pronounced structural disorder develops at the interface during the first 2 ps. Concurrently, numerous Ca and O atoms detach from their lattice sites in the CaO substrate and migrate toward the interfacial region, leading to severe disruption of the surface lattice. Simultaneously, this structural degradation accelerates the inward diffusion of C_3S species into the CaO, accompanied by a pronounced enrichment of C_3S at the CaO surface. Furthermore, the severe depletion of surface oxygen atoms precludes the formation of [SiO_4] tetrahedra.

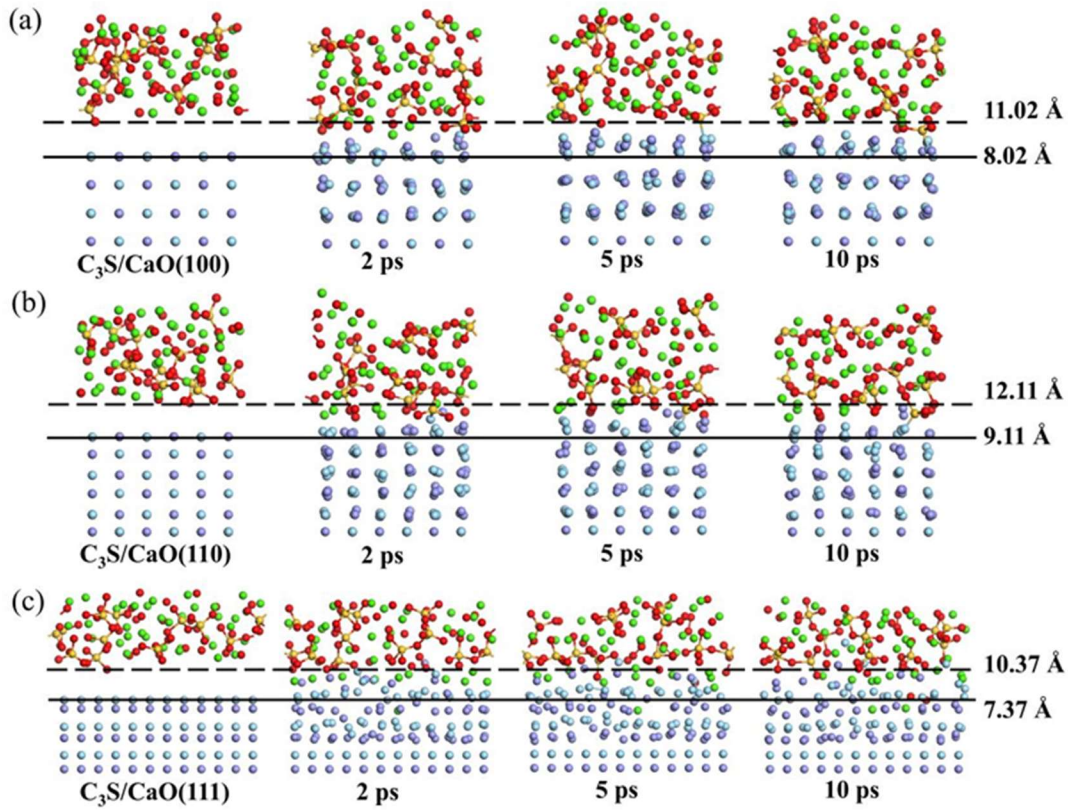


Figure 2. Atomic structural evolution of the C_3S/CaO interface: (**a**) C_3S/CaO(100), (**b**) C_3S/CaO(110) and (**c**) C_3S/CaO(111) (The solid and dashed horizontal lines mark the initial upper boundary of the CaO substrate and the lower boundary of the C_3S phase, respectively. Ca, Si, and O atoms in C_3S are shown in green, yellow, and red, while Ca and O atoms belonging to the CaO substrate are shown in purple and blue).

For the C_2S/CaO interface, a trend similar to the C_3S/CaO system was observed (Figure S6), although reactivity is attenuated due to the lower CaO content in C_2S. Specifically, the C_2S/CaO(100) interface exhibits the highest stability, whereas the C_2S/CaO(111) interface is the least stable; the C_2S/CaO(110) system displays intermediate behavior.

Figure 3 compares the atomic number density along the Z-axis for the C_3S/CaO(100), C_3S/CaO(110) and C_3S/CaO(111) systems over 8–10 ps. The solid and dashed reference lines denote the initial boundaries of the CaO substrate and the C_3S phase, respectively. For all three CaO orientations, the Ca and O density peaks in the CaO substrate become less pronounced and progressively broaden toward the interfacial region, indicating increasing disorder of the surface lattice.

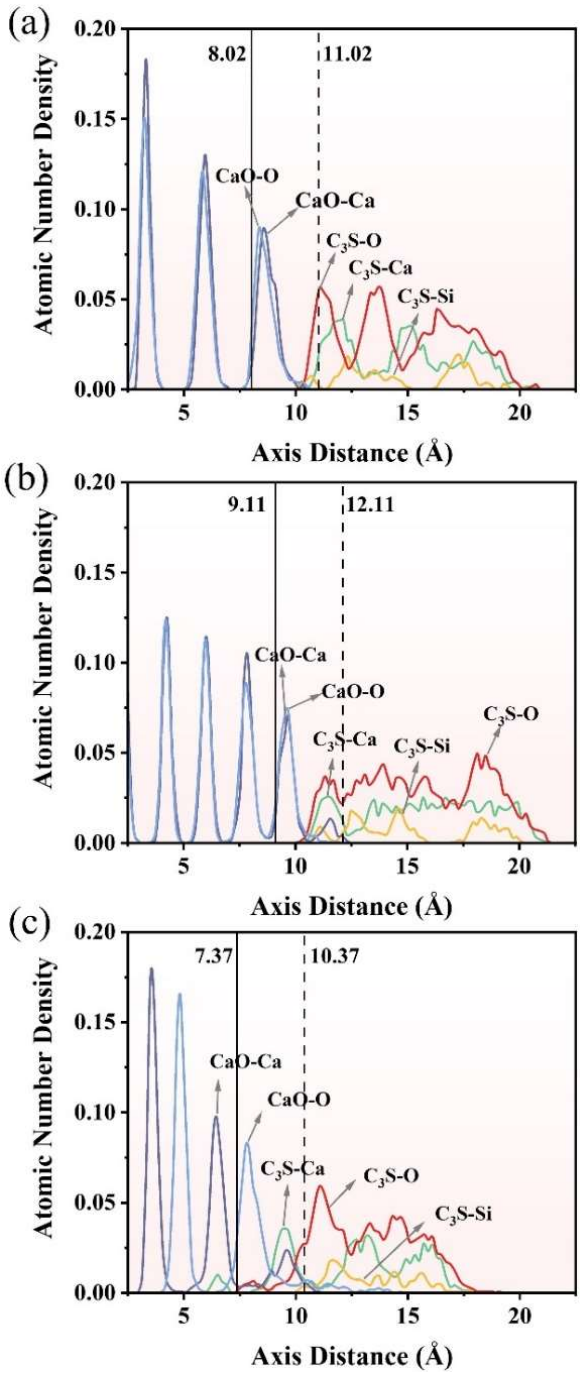


Figure 3. Atomic number density distribution of the C_3S/CaO interface: (**a**) C_3S/CaO(100), (**b**) C_3S/CaO(110) and (**c**) C_3S/CaO(111) (The solid and dotted reference lines mark the initial upper boundary of the CaO substrate and the lower boundary of the C_3S phase, respectively).

From C_3S/CaO(100) (Figure 3a) to C_3S/CaO(111) (Figure 3c), both the diffusion of atoms from CaO into C_3S and from C_3S into CaO gradually intensify. For the C_3S/CaO(100) case (Figure 3a), Ca and O atoms in CaO deviate from their initial positions and diffuse upward, in contrast, the downward diffusion of Ca, Si, and O atoms from C_3S into CaO is relatively limited. In the C_3S/CaO(110) case (Figure 3b), the Ca and O atoms from CaO also diffuse toward the C_3S side, with Ca exhibiting a greater diffusion extent. The Ca and O atoms from the C_3S phase show pronounced inward diffusion, suggesting that Ca atoms originating from C_3S tend to occupy lattice sites on the CaO(110) surface and form new structural units. For the C_3S/CaO(111) case (Figure 3c), Ca and O atoms from the CaO substrate diffuse outward and enter the C_3S region, while Ca, Si, and O from C_3S diffuse into the CaO substrate, with Ca exhibiting the most pronounced migration. The peak of the Ca density from C_3S coincides at 6.5 Å with the equilibrium positions of Ca atoms in the CaO lattice, indicating that during interfacial interdiffusion, Ca atoms from C_3S preferentially occupy the cation vacancies of the CaO lattice.

The results of atomic number density along the Z-axis for the C_2S/CaO systems over 8–10 ps are similar to C_3S/CaO systems. From C_2S/CaO(100) (Figure S7a) to C_2S/CaO(111) (Figure S7c), both the diffusion of atoms from CaO into C_2S and from C_2S into CaO gradually intensify. In the C_2S/CaO(111) case (Figure S7c), Ca, Si, and O atoms from the C_2S diffuse into the CaO substrate.

3.2. Evolution of the Interface Microstructure

As shown in Figure 4, the radial distribution functions (RDFs) of the C_3S/CaO interface during initial (0–2 ps) and final (8–10 ps) simulation stages are characterized by increased peak intensities and broadened peak widths. These changes indicate enhanced interfacial interactions, a higher probability of atomic bonding across the interface, and progressive structural disordering at the interface. Among the three crystallographic orientations, the C_3S/CaO(111) exhibits the most pronounced increases in the RDF peak intensities for both Ca(C_3S)–O(CaO) and Ca(CaO)–O(C_3S) pairs, demonstrating stronger mutual diffusion of Ca and O atoms across the C_3S/CaO(111) interface and consequently more intense interfacial interactions.

As shown in Figure S8, the RDFs of the C_2S/CaO interfaces during the initial (0–2 ps) and final (8–10 ps) simulation stages are characterized by increased peak intensities and broadened peak widths. The structural evolution of the C_2S/CaO systems is similar to that of the C_3S/CaO systems; specifically, the C_2S/CaO(111) system exhibits the most pronounced increases in the RDF peak intensities for both the Ca(C_2S)–O(CaO) and Ca(CaO)–O(C_2S) atomic pairs.

Figure 5 illustrates the interactions between Si atoms in the C_3S and the CaO. For the CaO(100) and CaO(110) surfaces, the close packed arrangement of surface oxygen atoms suppresses their outward diffusion into the C_3S phase, thereby providing anchoring sites for Si bond reconstruction. This facilitates the formation of new [SiO_4] tetrahedra at the interface via a bond dissociation and recombination mechanism, wherein Si atoms from the C_3S coordinate with surface oxygen atoms of the CaO substrate. In contrast, the inherently lower structural stability of the CaO(111) surface results in an increased reconstruction and disorder of surface oxygen. This, in turn, promotes the rapid diffusion of Ca atoms and further exacerbates the imbalance in diffusion kinetics between Ca and Si.

Figure S9 presents the interaction between Si atoms in C_2S and CaO. The formation of [SiO_4] tetrahedra at the interface is observed exclusively in the C_2S/CaO(110) system. This phenomenon can be attributed to two factors. First, the CaO(110) surface exhibits negligible outward diffusion of O atoms into the C_2S phase. Second, the presence of coordinatively unsaturated oxygen atoms on this surface drives the Si atoms in C_2S near the interface to bond with surface O atoms of CaO, thereby forming new stable tetrahedral structures at the interface.

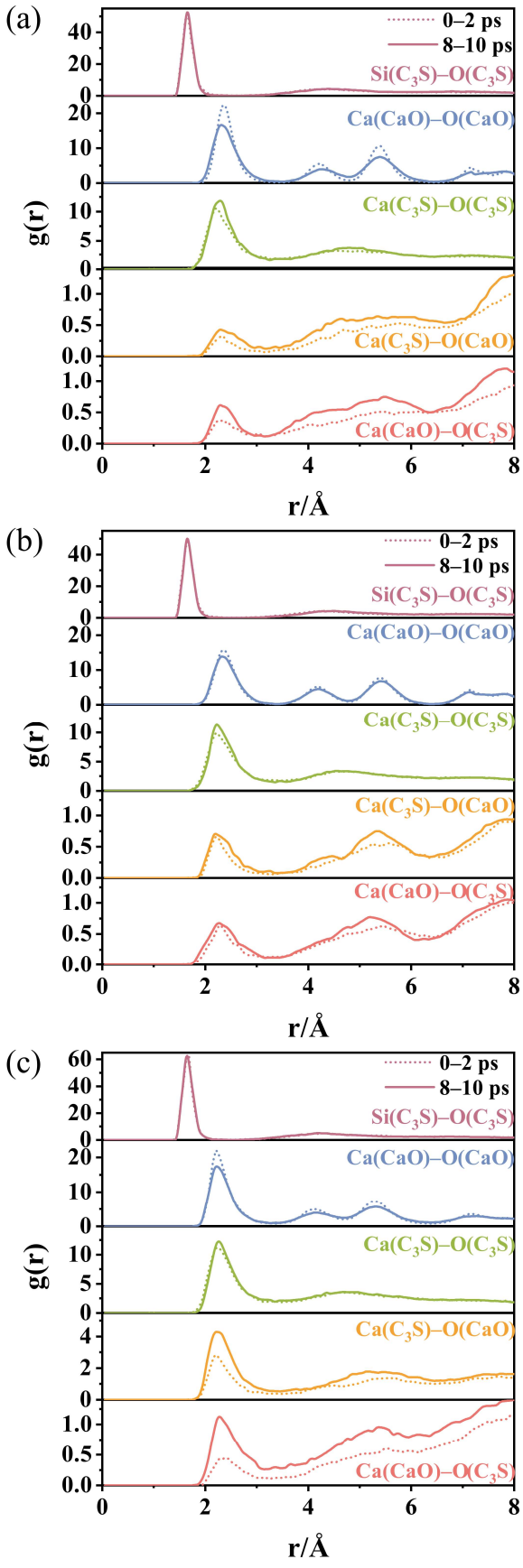


Figure 4. Radial distribution functions for the C_3S/CaO interfaces averaged over the early (0–2 ps, dotted lines) and final (8–10 ps, solid lines) stages of the simulated reaction: (**a**) C_3S/CaO(100), (**b**) C_3S/CaO(110) and (**c**) C_3S/CaO(111).

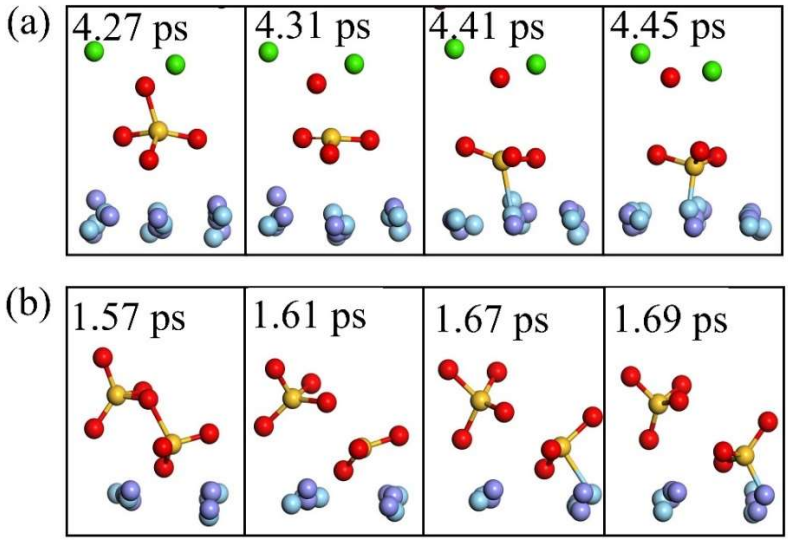


Figure 5. Interaction between Si atoms in C_3S and CaO: (**a**) C_3S/CaO(100) and (**b**) C_3S/CaO(110) (Ca, Si, and O atoms in C_3S are shown in green, yellow, and red, respectively, whereas Ca and O atoms in the CaO substrate are shown in purple and blue).

3.3. Comparison of Interfacial Interaction Energy

The interfacial interaction energies for the C_3S/CaO(100), C_3S/CaO(110), and C_3S/CaO(111) were quantified as a function of simulation time (Figure 6). The C_3S phase exhibits attractive interactions with all three CaO surfaces, with the magnitude of the interaction energy following the sequence: C_3S/CaO(111) > C_3S/CaO(110) > C_3S/CaO(100). The relatively low interaction magnitude of the C_3S/CaO(100) indicates a weak tendency for interfacial reaction, which corroborates the limited atomic diffusion observed in the density profiles. The C_3S/CaO(110) displays intermediate interaction energy. In contrast, the C_3S/CaO(111) interface is the least stable, showing the strongest propensity for chemical reactions between the two phases.

The interfacial interaction energies of C_2S/CaO(100), C_2S/CaO(110), and C_2S/CaO(111) were quantified as a function of simulation time (Figure S10). The trends observed for the C_2S/CaO systems are similar to C_3S/CaO systems. C_2S exhibits attractive interactions with all three CaO surfaces, with the interaction energy following the order: C_2S/CaO(111) > C_2S/CaO(110) > C_2S/CaO(100).

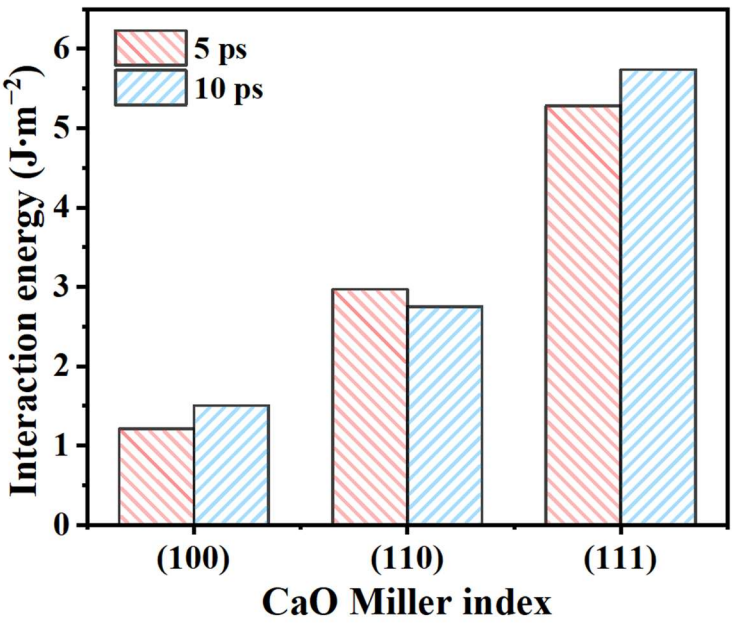


Figure 6. Interaction energies of C_3S and CaO surface with different Miller indices.

3.4. Charge Distribution and Transfer

Charge density difference analysis enables direct visualization of interfacial charge redistribution, thereby providing electronic scale evidence for the interfacial bonding and reactions. Differential charge distribution analysis (1D and 3D) of the C_3S/CaO interface at 10 ps was performed (Figure 7), where yellow and cyan isosurfaces denote charge accumulation and depletion regions, respectively.

In the C_3S/CaO(100) and C_3S/CaO(110) (Figure 7a,b), limited charge transfer occurs between Ca and O atoms at the interface, indicating weak interdiffusion between C_3S and CaO. The Si atoms from C_3S bond with O atoms from CaO, with electron density accumulating predominantly around the oxygen atoms, confirming electron transfer from Si (in C_3S) to O (in CaO). In contrast, the C_3S/CaO(111) case (Figure 7c) exhibits extensive charge transfer at the interface, primarily driven by mutual diffusion between Ca and O atoms from both CaO and C_3S. Specifically, electron transfer proceeds bidirectionally: from the substrate Ca to the clinker O, and conversely, from the clinker Ca to the substrate O. This bidirectional charge exchange mechanism results in a significantly greater magnitude of charge transfer for the CaO(111) facet compared to that of the (100) and (110) cases.

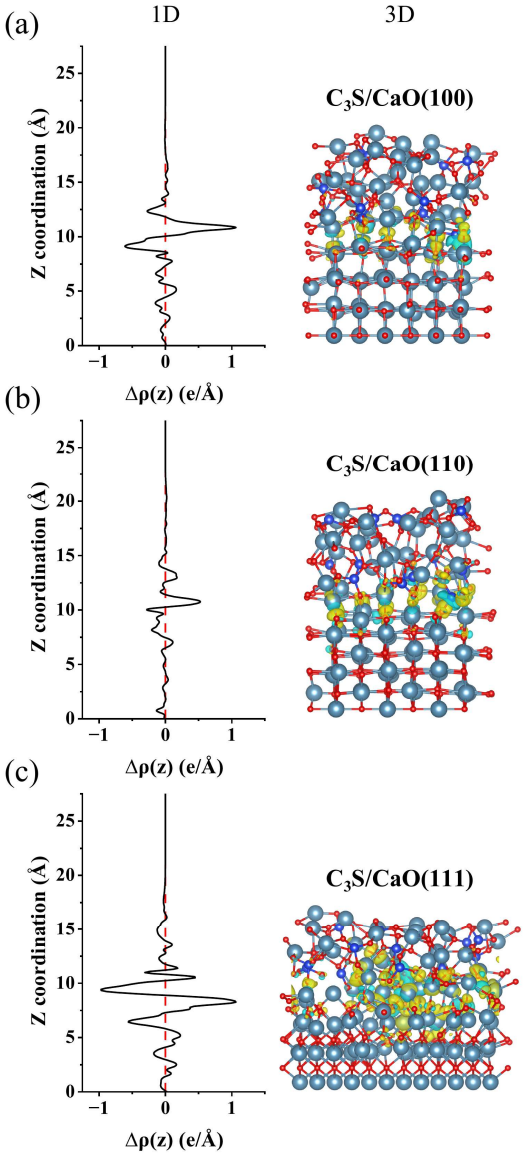


Figure 7. One-dimensional and three-dimensional differential charge density diagrams of the C_3S/CaO interface: (**a**) C_3S/CaO(100), (**b**) C_3S/CaO(110) and (**c**) C_3S/CaO(111) (Si, Ca, and O atoms are shown in blue, gray, and red, respectively. Yellow and cyan isosurfaces denote electron accumulation and electron depletion, respectively. The isosurface level is 0.005 e/bohr^3).

The Bader charges for the C_3S/CaO case at the 10 ps snapshot were calculated (Table 1), where positive and negative values denote electron depletion and accumulation, respectively. For the C_3S/CaO(100) case, the CaO substrate exhibits a net electron depletion of 0.72 e. In the C_3S/CaO(110) case, this electron depletion becomes more pronounced, reaching 1.70 e. This behavior is primarily driven by charge transfer from the Ca atoms within the CaO phase. Analysis of the charge transfer pathways reveals that at both the (100) and (110) interfaces, Ca atoms in the substrate transfer electrons to the C_3S. Concurrently, Si and Ca atoms from the C_3S phase transfer electrons back to the O atoms in the CaO substrate. However, this reverse charge transfer is insufficient to compensate for the initial electron depletion from CaO. Consequently, the interfacial reactivity of the CaO(100) and CaO(110) facets is predominantly governed by electron donation from the Ca atoms in the substrate to the C_3S. In contrast, the C_3S/CaO(111) case exhibits a reversed electron transfer, characterized by a substantial net charge transfer of 5.48 e from C_3S to CaO. This is mainly attributed to the strong interaction between the Ca atoms in the clinker and the surface O atoms of the CaO(111) plane. This pronounced charge transfer induces Coulombic potential distortion, which not only amplifies the interfacial polarization effect but also significantly facilitates atomic mutual diffusion.

The Bader charges of Ca and O atoms in the CaO region of the C_3S/CaO interfaces are listed in Table S3. The magnitudes of the effective charges are found to decrease in the order CaO(100) > CaO(110) > CaO(111). The reduced effective charges of Ca and O atoms on CaO(111) suggest weakened ionic interactions and a lower Ca–O bonding strength, thereby decreasing the structural stability of the CaO lattice. During interfacial reactions with C_3S, the Ca–O bonds on the CaO(111) surface are therefore more susceptible to disruption, resulting in greater interfacial reactivity. This interpretation is consistent with the pronounced charge transfer observed at the C_3S/CaO(111) interface (Table 1). Consequently, under the simulated high-temperature conditions, the CaO(111) surface exhibits a greater tendency toward surface destabilization and structural degradation.

Differential charge distribution analysis (1D and 3D) of the C_2S/CaO interface at 10 ps was presented (Figure S11). In the C_2S/CaO systems, the extent of charge transfer follows the order: C_2S/CaO(111) > C_2S/CaO(110) > C_2S/CaO(100). Bader charges for C_2S with CaO systems at 10 ps were calculated (Tables S4 and S5). Positive values denote electron loss; negative values indicate electron gain. For the C_2S/CaO(100) system, a net charge transfer of 1.91 e occurs from CaO to C_2S. For the C_2S/CaO(110) system, CaO transfers 0.70 e to C_2S. Although the C_2S/CaO(110) interface exhibits stronger interfacial interaction than the C_2S/CaO(100) interface, its net Bader charge transfer is smaller. This apparent contradiction arises because, in the C_2S/CaO(110) system, the interaction between Si atoms from C_2S and O atoms from CaO generates more pronounced reverse electron transfer, thereby reducing the overall electron loss from CaO. In contrast, for the C_2S/CaO(111) system, a net charge transfer of 3.07 e is observed from C_2S to CaO, which is attributed to the strong interaction between Ca atoms in C_2S and O atoms on the CaO(111) surface.

Table 1. Bader charges of the C_3S/CaO interface (Positive values denote electron loss, negative values denote electron gain).

Model	C_3S (e)	CaO (e)
C_3S/CaO(100)	−0.72	0.72
C_3S/CaO(110)	−1.70	1.70
C_3S/CaO(111)	5.48	−5.48

3.5. Comparison with Experimental Observations and Limitations

The present AIMD results are compared with experimental studies. For example, Qiu et al. [18] reported that C_2S can react with free CaO to form a high melting point C_3S rich layer, which inhibits the inward penetration of corrosive species such as Fe_2O_3 and Al_2O_3. This experimental observation is qualitatively consistent with our simulations, in which Si-containing clinker species interact with surface

O atoms of CaO through Si–O bond reconstruction and form new [SiO_4] tetrahedral units at the C_3S/CaO and C_2S/CaO interfaces. These newly formed silicate units provide an atomic-scale explanation for the development of Ca rich silicate reaction structures at the refractory clinker interface. Similarly, Rodríguez-Galicia et al. [19] experimentally observed penetration of liquid clinker along pores and grain boundaries followed by the formation of a dense reaction layer. Although the present AIMD simulations cannot reproduce the micrometer-scale penetration process because of their limited spatial and temporal scales, the atomic interdiffusion and interfacial bonding processes identified here represent elementary events that can contribute to the formation and evolution of such reaction layers.

The scope of this comparison is also limited by the simulation conditions. The present models contain idealized CaO surfaces and simplified C_3S or C_2S compositions, with interfacial evolution followed for 10 ps at 1873 K. Practical refractories contain multiple phases, defects, pores, and grain boundaries and experience longer exposure times and varying temperatures. The comparison therefore supports qualitative mechanistic consistency, rather than quantitative validation of corrosion rates, penetration depths, or reaction-layer thicknesses. In particular, the previous experiments do not directly establish the relative reactivities of the CaO(100), CaO(110), and CaO(111) facets. The predicted orientation dependence and its possible implications for kiln-coating stability require further experimental assessment.

4. Conclusions

The atomic-scale interaction mechanism between C_3S/C_2S and CaO interfaces ((100), (110), and (111)) was systematically investigated via *ab initio* molecular dynamics simulations. The key findings are as follows:

(1) The CaO(100) surface maintains structural integrity through limited atomic bonding and charge transfer with C_3S and C_2S. In contrast, the CaO(111) interface exhibited intense, bidirectional atomic interdiffusion, significant surface disordering, and the highest surface energy (3.88 $J \cdot m^{-2}$), confirming its high susceptibility to corrosive attack.

(2) For the low surface energy CaO(100) and CaO(110) facets, both C_3S and C_2S form [SiO_4] tetrahedra through Si–O bonding, which effectively suppresses the dissolution of CaO. In contrast, the CaO(111) facet, characterized by high surface energy, structural instability, and strong interfacial polarization, undergoes vigorous interfacial reactions, making the refractory more susceptible to corrosion.

(3) The CaO(110) surface exhibits an intermediate level of interfacial reactivity between the relatively inert CaO(100) and highly reactive CaO(111) surfaces. This moderate interaction promotes interfacial Si–O bond reconstruction while avoiding the severe lattice degradation observed for CaO(111). Therefore, CaO(110) may provide a favorable balance between clinker and refractory interfacial bonding and preservation of the refractory, suggesting its potential relevance to stable kiln coating formation. Nevertheless, this implication remains a theoretical prediction and requires further experimental validation.

(4) From an engineering perspective, controlling the population of exposed CaO facets may provide a potential route for tailoring clinker and refractory interactions. Because the CaO(110) surface possesses a higher surface energy than CaO(100), preferential exposure of CaO(110) is unlikely to arise solely from equilibrium crystal growth. Instead, future studies may explore non equilibrium microstructural regulation through control of raw material grain morphology, element doping, and sintering parameters. These strategies should be experimentally evaluated to determine whether an increased fraction of exposed CaO(110) surfaces can be realized in practical MgO–CaO refractories and whether such microstructural regulation contributes to improve the stability kiln coating.

Supplementary Materials

The following supporting information can be found at: https://www.sciepublish.com/article/pii/1299, Figure S1. XRD calculated patterns of CaO crystals; Figure S2. Different crystal face models of CaO: (a) CaO(100), (b) CaO(110) and (c) CaO(111) (Ca and O atoms are represented by purple and blue spheres, respectively); Figure S3. Variations of system temperature (a) total energy of C_3S and C_2S melt at 1873 K; (b) during AIMD simulations of C_3S and C_2S melt at 1873 K; Figure S4. Cutoff-energy convergence test for the C_3S/CaO(100) system; Figure S5. Surface energies of different crystal faces of CaO; Figure S6. Atomic structural evolution of the C_2S/CaO interface: (a) C_2S/CaO(100), (b) C_2S/CaO(110) and (c) C_2S/CaO(111)(The solid and dotted lines represent the upper surface of the CaO and the lower surface of C_2S in the initial interface model, respectively; Ca, Si and O atoms in the C_2S are represented by green, yellow and red spheres, respectively; Ca and O atoms in CaO are represented by purple and blue spheres, respectively); Figure S7. Atomic number density distribution of the C_2S/CaO interface: (a) C_2S/CaO(100), (b) C_2S/CaO(110) and (c) C_2S/CaO(111) (The solid and dotted lines are the upper surface of the CaO and the lower surface of C_2S in the initial interface model, respectively); Figure S8. Radial distribution functions of the C_2S/CaO interface at the initial (0–2 ps, dotted lines) and final (8–10 ps, solid lines) stages of the simulated reaction: (a) C_2S/CaO(100), (b) C_2S/CaO(110) and (c) C_2S/CaO(111); Figure S9. Interaction mechanism between Si atoms in C_2S and CaO(110) (Ca and O atoms in CaO are represented by purple and blue spheres, respectively; Ca, Si and O atoms in C_2S are represented by green, yellow and red spheres, respectively); Figure S10. Interaction energies of C_2S and CaO surface with different Miller indices; Figure S11. One-dimensional and three-dimensional differential charge density of the C_2S/CaO interface: (a) C_2S/CaO(100), (b) C_2S/CaO(110) and (c) C_2S/CaO(111) (Si, Ca and O atoms are represented by blue, cyan and red balls respectively; yellow and cyan represent the regions of electron accumulation and loss respectively; the isosurface value is 0.005 e/bohr^3); Table S1. The Optimized and experimental lattice parameters [40]; Table S2. Atomic counts in the simulated systems of C_3S and C_2S; Table S3. Average Bader charge values of atoms at the C_3S/CaO interface (Positive values denote electron loss, negative values denote electron gain); Table S4. Bader charges of C_2S/CaO interface (Positive values denote electron loss, negative values denote electron gain); Table S5. Average Bader charge values of atoms at the C_2S/CaO interface (Positive values denote electron loss, negative values denote electron gain).

Statement of the Use of Generative AI and AI-Assisted Technologies in the Writing Process

During the preparation of this manuscript, the author used ChatGPT and Deepseek software to polish the English. After using this tool/service, the authors reviewed and edited the content as needed and take full responsibility for the content of the published article.

Acknowledgments

The authors are grateful for the financial support from the National Natural Science Foundation of China and the Scientific Research Project of the Department of Education of Hubei Province. We also acknowledge support from the High-Performance Computing Center of Wuhan University of Science and Technology.

Author Contributions

Q.C.: Visualization, Formal analysis, Writing—original draft. Y.X.: Investigation, Methodology, Formal analysis, Visualization. L.H.: Methodology, Formal analysis, Writing—review & editing, Validation, Conceptualization, Supervision, Funding acquisition. H.Z.: Writing—review & editing, Resources, Project administration, Conceptualization, Supervision, Funding acquisition. S.Z.: Funding acquisition, Resources, Writing—review & editing.

Ethics Statement

Not applicable.

Informed Consent Statement

Not applicable.

Data Availability Statement

The data supporting this study are available from the corresponding authors upon reasonable request.

Funding

This research was funded by the National Natural Science Foundation of China (Grant No. U23A20559, 52372030, 52272021 and 52232002) and the Scientific Research Project of the Department of Education of Hubei Province (D20251105).

Declaration of Competing Interest

The authors declare that they have no known competing financial interests or personal relationships that could have appeared to influence the work reported in this paper.

References

1. Xu L, Chen M, Huang WJ, Wang N, Dong JH, Yin XL. Effects of CaO content on sintering and lightweight of Al_2O_3-MgO–CaO refractories. *Mater. Res. Innov.* **2015**, *19*, 212–217. DOI:10.1179/1432891714z.0000000001080
2. Ren B, Li Y, Jin S, Sang S. Correlation between chemical composition and alkali attack resistance of bauxite-SiC refractories in cement rotary kiln. *Ceram. Int.* **2017**, *43*, 14161–14167. DOI:10.1016/j.ceramint.2017.07.157
3. Ghasemi-Kahrizsangi S, Dehsheikh HG, Karamian E, Boroujerdnia M, Payandeh K. Effect of $MgAl_2O_4$ nanoparticles addition on the densification and properties of MgO–CaO refractories. *Ceram. Int.* **2017**, *43*, 5014–5019. DOI:10.1016/j.ceramint.2017.01.011
4. Chen X, Xie J, Mei S, He F. NOx and SO_2 Emissions during Co-Combustion of RDF and Anthracite in the Environment of Precalciner. *Energies* **2018**, *11*, 337. DOI:10.3390/en11020337
5. Shahraki A, Ghasemi-Kahrizsangi S, Nemati A. Performance improvement of MgO–CaO refractories by the addition of nano-sized Al_2O_3. *Mater. Chem. Phys.* **2017**, *198*, 354–359. DOI:10.1016/j.matchemphys.2017.06.026
6. Li S, Yin Z, Wang A, Yu C, Feng R, Liu G, et al. Characterization, Exploitation and Application of Tibetan Microcrystalline Magnesite. *High-Temp. Mater.* **2024**, *1*, 10007. DOI:10.70322/htm.2024.10007
7. Li Y, Huang Z, Dong L, Liu X, Yuan G, Lei H, et al. Carbon nanotubes-functionalized MgO-based castables: Super-nonwetting behavior and slag corrosion resistance. *Constr. Build. Mater.* **2024**, *442*, 137601. DOI:10.1016/j.conbuildmat.2024.137601
8. Wang YX, Li YG, Gao YB, Huang Z, Zhang HJ. High-temperature wetting behavior between slag and refractory. *J. Iron Steel Res. Int.* **2024**, *31*, 1304–1319. DOI:10.1007/s42243-024-01252-z
9. Qu C, Huang X, Zhang H, Li Y, Zhang S. High-temperature wettability to slag of carbon nanotube modified MgO castable prepared by a chemical vapor deposition method. *Ceram. Int.* **2025**, *51*, 63688–63695. DOI:10.1016/j.ceramint.2025.10.463
10. Meng KY, Wu XW, Zheng LG, Wang LX, Min X, Fang MH, et al. Pore-structure regulation of MgO–CaO microporous refractory aggregates. *Ceram. Int.* **2026**, *52*, 11619–11629. DOI:10.1016/j.ceramint.2026.01.320
11. Wu G, Yan W, Schafföner S, Lin X, Ma S, Zhai Y, et al. Effect of magnesium aluminate spinel content of porous aggregates on cement clinker corrosion and adherence properties of lightweight periclase-spinel refractories. *Constr. Build. Mater.* **2018**, *185*, 102–109. DOI:10.1016/j.conbuildmat.2018.07.058
12. Bakiyeva Z, Lisitsyn V, Alpysova G, Karnaukhova A, Mussakhanov D, Afanasyev D, et al. Peculiarities of Radiation Synthesis of $MeWO_4$ Ceramics. *High-Temp. Mater.* **2026**, *3*, 10008. DOI:10.70322/htm.2026.10008
13. Zhou W, Zhang L, Zhang Z, Ji X, Liu X, Li C, et al. Mullite-Corundum-Al_2TiO_5 Foamed Ceramics with Extremely Low Thermal Conductivity Induced by Multiple Thermal Resistance. *High-Temp. Mater.* **2026**, *3*, 10011. DOI:10.70322/htm.2026.10011

14. Simoni M, Hanein T, Duvallet TY, Jewell RB, Provis JL, Kinoshita H. Producing cement clinker assemblages in the system: CaO-SiO_2-Al_2O_3-SO_3-$CaCl_2$-MgO. *Cem. Concr. Res.* **2021**, *144*, 106418. DOI:10.1016/j.cemconres.2021.106418
15. Wagri NK, Carlborg M, Eriksson M, Ma C, Broström M, Andersson BM. High temperature interactions between coal ash and MgO-based refractories in lime kiln conditions. *Fuel* **2023**, *342*, 127711. DOI:10.1016/j.fuel.2023.127711
16. Wu N, Zeng L, Fu T, Chen J, Zhang F, Zeng Y, et al. The Rapid Boiling of Thin Liquid Films with Different Thicknesses on Nanochannel Copper Plates: A Molecular Dynamics Study. *Coatings* **2023**, *13*, 2057. DOI:10.3390/coatings13122057
17. Hou XS, Chen JF, Cao YP, Liu GP, Wei GP, Yan W, et al. Influence of bonding systems on the properties of Al_2O_3-MgO refractory castables: Aluminate cement and alumina silica gel. *Ceram. Int.* **2024**, *50*, 46695–46704. DOI:10.1016/j.ceramint.2024.09.021
18. Qiu GB, Peng B, Li X, Hou XM, Guo M, Zhang M. Properties of regenerated MgO–CaO refractory bricks: Impurity of silicon dioxide. *Mater. Res. Innov.* **2015**, *19*, S2-119–S2-124. DOI:10.1179/1432891714z.0000000001066
19. Rodríguez-Galicia JL, de Aza AH, Rendón-Angeles JC, Pena P. The Mechanism of corrosion of MgO-$CaZrO_3$-calcium silicate materials by cement clinker. *J. Eur. Ceram. Soc.* **2007**, *27*, 79–89. DOI:10.1016/j.jeurceramsoc.2006.01.014
20. Wu Z, Dong B, Peng G, Luo W, Shan X, Nie L, et al. Novel insight into the self-lubricating mechanism of Cu–Pb bearing alloy during sliding friction with the guidance of molecular dynamics. *J. Mater. Res. Technol.* **2023**, *24*, 3157–3163. DOI:10.1016/j.jmrt.2023.03.163
21. Yu J, Yu F, Fu Q, Zhao G, Gong C, Wang M, et al. Combining Machine Learning and Molecular Dynamics to Predict Mechanical Properties and Microstructural Evolution of FeNiCrCoCu High-Entropy Alloys. *Nanomaterials* **2023**, *13*, 968. DOI:10.3390/nano13060968
22. Zhou J, Lu Y, Wang C, Feng D, Zhang H, Li Y. Molecular dynamics study of graphene-coated reinforced tribomechanical properties: Hard versus soft substrates. *Comput. Mater. Sci.* **2023**, *226*, 112209. DOI:10.1016/j.commatsci.2023.112209
23. Liu X, Dong L, Xing Y, Huang L, Zhang H, Zhang S. Interaction between MgO and molten Fe: Roles of crystal orientation, surface defects, and oxygen in melt. *Surf. Interfaces* **2025**, *73*, 107617. DOI:10.1016/j.surfin.2025.107617
24. Chen J, Huang L, Dong L, Zhang H, Huang Z, Li F, et al. Hydration behavior of MgO surface: A first-principles study. *Appl. Surf. Sci.* **2023**, *611*, 155441. DOI:10.1016/j.apsusc.2022.155441
25. Qi Y, Liu X, Dong L, Huang L, Zhang H, Zhang S, et al. High-temperature wettability and interfacial interaction between CaO-MgO-Al_2O_3-SiO_2-Fe_2O_3 slag and MgO. *Appl. Surf. Sci.* **2026**, *731*, 166452. DOI:10.1016/j.apsusc.2026.166452
26. Xing Y, Zhang R, Chen J, Dong Z, Zhang H, Huang L. Atomic-Level Insights into the HfB_2 Oxidation Mechanism by the Combination of Density Functional Theory and *Ab Initio* Molecular Dynamics Calculations. *Inorg. Chem.* **2026**, *65*, 13063–13074. DOI:10.1021/acs.inorgchem.6c01325
27. Hu Y, Liu X, Chen J, Huang L, Zhang H, Zhang S, et al. Stepwise Oxidation Mechanisms of h-BN: Effect of Zigzag Edge and Armchair Edge. *J. Am. Ceram. Soc.* **2026**, *109*, e70764. DOI:10.1111/jace.70764
28. Liu X, Dong L, Huang L, Zhang H, Zhang S. Atomic-Scale Insights into High-temperature Interfacial Interactions between Molten Al and MgO. *J. Am. Ceram. Soc.* **2026**, *109*, e70305. DOI:10.1111/jace.70305
29. Zhang L, Xing Y, Zhang H, Huang L, Zhang S. *Ab Initio* Molecular Dynamics Study of CMAS Slag–MgO Interfaces: Crystal Orientation Effects and Corrosion Mechanisms. *J. Am. Ceram. Soc.* **2026**, *109*, e70793. DOI:10.1111/jace.70793
30. Monkhorst HJ, Pack JD. Special points for Brillouin-zone integrations. *Phys. Rev. B* **1976**, *13*, 5188–5192. DOI:10.1103/physrevb.13.5188
31. Kresse G, Hafner J. *Ab initio* molecular dynamics for open-shell transition metals. *Phys. Rev. B* **1993**, *48*, 13115–13118. DOI:10.1103/physrevb.48.13115
32. Blöchl PE. Projector augmented-wave method. *Phys. Rev. B* **1994**, *50*, 17953–17979. DOI:10.1103/physrevb.50.17953
33. Perdew JP, Wang Y. Accurate and simple analytic representation of the electron-gas correlation energy. *Phys. Rev. B* **1992**, *45*, 13244–13249. DOI:10.1103/physrevb.45.13244
34. Perdew JP, Burke K, Ernzerhof M. Generalized Gradient Approximation Made Simple. *Phys. Rev. Lett.* **1996**, *77*, 3865–3868. DOI:10.1103/physrevlett.77.3865
35. Nosé S. A unified formulation of the constant temperature molecular dynamics methods. *J. Chem. Phys.* **1984**, *81*, 511–519. DOI:10.1063/1.447334
36. Weiss R, Schmidt A, Miller GA, Barnea N. Short-range correlations and the charge density. *Phys. Lett. B* **2019**, *790*, 484–489. DOI:10.1016/j.physletb.2019.01.053
37. Henkelman G, Arnaldsson A, Jónsson H. A fast and robust algorithm for Bader decomposition of charge density. *Comput. Mater. Sci.* **2006**, *36*, 354–360. DOI:10.1016/j.commatsci.2005.04.010
38. Wang V, Xu N, Liu J-C, Tang G, Geng W-T. VASPKIT: A user-friendly interface facilitating high-throughput computing and analysis using VASP code. *Comput. Phys. Commun.* **2021**, *267*, 108033. DOI:10.1016/j.cpc.2021.108033

39. Momma K, Izumi F. VESTA 3 for three-dimensional visualization of crystal, volumetric and morphology data. *J. Appl. Crystallogr.* **2011**, *44*, 1272–1276. DOI:10.1107/s0021889811038970
40. Lide DR. *CRC Handbook of Chemistry and Physics*; CRC Press: Boca Raton, FL, USA, 2004; pp. 255–256.